Size effect of accelerated seismic release from failures under compression in naturally fractured media

Rui Wu, Fuqiang Gao,[*] Xiangyuan Peng, Shuangyong Dong, and Shuwen Cao

CCTEG Coal Mining Research Institute, Beijing, China
and State Key Laboratory of Intelligent Coal Mining and Strata Control, Beijing, China

Bing Qiuyi Li

Department of Civil and Environmental Engineering, Western University, London, Canada

It is crucial to understand the scaling behaviors of acoustic emissions (AEs) preceding damage localization in order to predict failures of brittle solids under compression. Yet, the effect of length scale on the complex interplay between the initiation, propagation, and coalescence of pre-existing fracture networks and corresponding AE behaviors is poorly understood. In this study, we perform laboratory compressional experiments on naturally fractured rocks at four sample sizes from 50 to 300 mm whose strength generally exhibits a finite-size effect. We analyze the time history of AE energy distribution and accelerated seismic release (ASR) until catastrophic failures of the specimens. We find their time evolution towards failure resembles the observations from specimens containing a single fault and highly microstructurally disordered materials. We observe clear evidence that a size effect exists at small AE magnitude, where larger specimens tend to produce a higher proportion of smaller microcracks. However, the AE energy distribution is scale-independent at high energies. Near to failure, the power-law component of the AE energy population is almost stationary. The temporal evolution of the AE activity rate is independent of sample size; instead, there exist fast and slow periods of the AE activity rate that could be attributed to the stress heterogeneities around the fracture network. ASRs are exclusively observed in the AE activity rate and are more general in the lack of criticality. Our interpretation of observed foreshock activities at varying sample sizes in fractured media may have significance for understanding and predicting failures from natural hazards and engineering instabilities.

I. INTRODUCTION

Brittle failure under compression is ubiquitous across natural catastrophes, engineering disasters, and both materials and life sciences. Examples include earthquakes [1,2], landslides [3], volcanic eruptions [4], mine rock bursts [5], borehole/tunnel collapses [6,7], as well as bone fractures [8]. Such failures are triggered when the stress level exceeds a critical threshold, often accompanied by transient elastic waves emitted from the fracture defects [9]. These fracture-induced elastic waves, known as acoustic emissions (AEs), represent foreshock activities that exhibit scale-independent statistics among energy, occurrence frequency, and distances to failure [10,11]. For instance, the relationship between AE energy and occurrence frequency, termed AE energy population, typically adheres to a power-law distribution whose exponent ϵ could decrease as the system approaches failure [12–14]. In parallel, as the system approaches the failure, the overall AE energy rate or AE activity rate is expected to increase, usually following a power-law evolution, also referred to as accelerated seismic release (ASR) [15]. The time evolution in exponent ϵ and ASR as the system approaches failure

reflects the transition from microcrack coalescence to the nucleation of faulting. The failure can be abrupt and critical if the material microstructure exhibits a very small amount of heterogeneity, such as in glass [16,17] and granite [12]. This failure is marked by a discontinuous or first-order transition between intact and failed states marked by an abrupt decrease in exponent ϵ. The ASRs dominate exceedingly close to catastrophic failure, with their statistics diverging at characteristic time and length scales, which complicates the prediction of such catastrophic events [11,18].

In contrast to homogeneous solids, brittle fracture usually occurs in solids that manifest inherent heterogeneity across a spectrum of length scales in many materials such as rock, coal, concrete, ice, ceramic, and bone. The heterogeneity is identified as the main cause of the observed size effect on material strength, supported by extensive experimental and analytical studies [19,20]. The size effect conforms to a suite of scaling laws, derived from either deterministic energetic approaches [19] or weakest-link theory underpinned by extreme value statistics [21–23]. The increased heterogeneity tends to modulate the failure from discontinuous or first-order to continuous or second-order phase transition at the macroscopic failure point [24–26]. This transition is accompanied by a shift in the intermittent collective dynamics of AEs which often precede the onset of material failure. These activities manifest
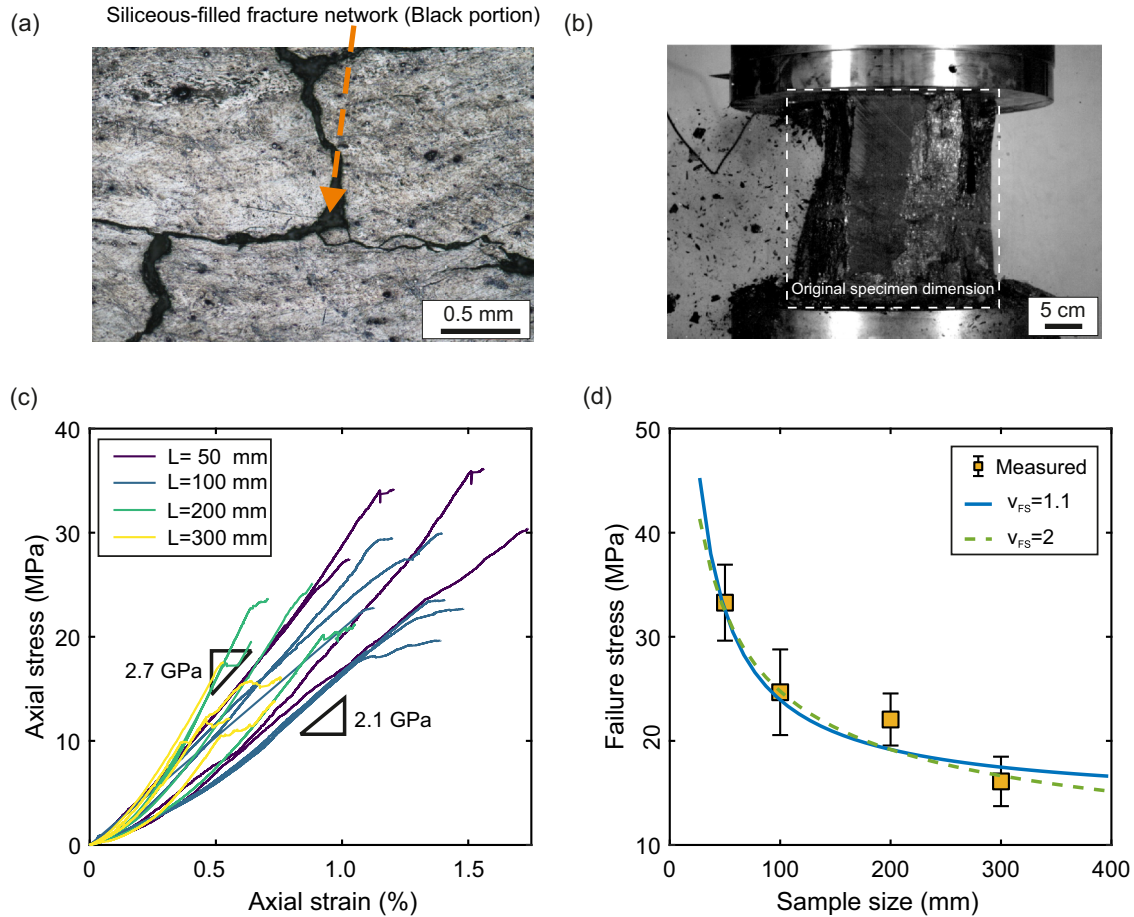
---

[*]Contact author: fuqgao@gmail.com

FIG. 1. (a) Microscopic observation of thin sections (thickness: $30 \pm 5\,\mu m$) utilizing reflected light oil immersion microscopy, highlighting dark areas indicative of silica-filled fractures. (b) Specimen ($L = 300$ mm) at 95% peak load captured by a high-speed camera. (c) Stress-strain results of 20 uniaxial compression tests across varying specimen sizes ($L = 50, 100, 200, 300$ mm). (d) Size-dependent failure stress, denoted by standard deviations (orange), alongside the theoretical prediction based on finite-size scaling considering ν_{FS} equals 1.1 and 2, respectively.

as sequences of discrete events, frequently termed avalanches [27], indicating a complex interplay between material heterogeneity and microcracking mechanism.

Laboratory investigations have focused on the intermittent dynamics of heterogeneous materials characterized by a range of microstructural disorders such as pore structure [16,26,28,29], microcracks [30], grain or aggregate sizes [31,32], composition [28], and cellular structure [33,34], in parallel with specimen-scale heterogeneities such as a preexisting notch [35,36]. It was found that an increase in heterogeneity of highly porous glass can cause a significant increase in foreshock activities, leading to the improvement in the predictability of the time to failure [17]. Furthermore, after the introduction of micrometre-scale microcrack networks to "crack-free" granite through heating/cooling treatments, Cartwright-Taylor et al. [37] found that heated granite exhibited characteristics of a second-order transition, in contrast to the first-order transition observed in untreated granite.

In a recent study, Patton et al. [36] revealed that granite containing a single centimetre-scale pre-cut notch could fail without criticality, accompanied by minor fluctuations of AE energy distribution at failure, unlike the clear decreasing trend in intact granite. Nevertheless, little attention has been paid to the role of pre-existing fractures and fracture networks [38],

representing a system of structural heterogeneities and controlling the structural strength on the intermittent AE dynamics of failure under compressive load. It is not yet clear how AE statistics evolve temporally in such fractured media and whether AE statistics behave similarly to those in materials containing a single large pre-existing fracture [35,36]. Moreover, Vu et al. [32] found that the critical exponents governing the AE statistics in concrete were found to be independent of sample size. Nevertheless, it is not known whether this observation applies to fractured rocks. In this research, we further investigate AE statistics in well-characterized fractured rock with varying sample sizes under compression, aiming to understand the temporal evolution and scale dependence of AE statistics under the existence of fracture networks.

II. MATERIALS AND METHODS

A. Material description

We used coal as a fractured medium in this study. The coal is collected from large blocks (approximately $0.2\,m^3$) cut from the Hejiata Coal Mine in Yulin, Shaanxi, China. The bulk density of the coal is $1.30 \pm 0.01\,g/cm^3$ under ambient conditions. In Fig. 1(a), the examination of thin sections reveals a heterogeneous microstructure characterized

by highly developed, pervasive fracture networks. The light regions represent the surrounding matrix, primarily organic materials, shale, hematite, etc. In contrast, the dark areas reveal the pattern and distribution of silica-filled fractures whose compositions significantly differ from the matrix. These interconnected fracture networks exhibit a characteristic aperture up to several tens of micrometers and lengths spanning from several millimeters to several centimeters visible to the eye. Measurements of Young's modulus and Poisson's ratio are conducted through standard uniaxial compression tests on six cylindrical specimens (diameter: 50 mm, length: 100 mm), yielding values of approximately 2.4 ± 0.3 GPa and 0.24 ± 0.03, respectively.

B. Uniaxial compressive test

A set of 20 specimens is prepared into cubic shapes with sizes increasing incrementally ($L = 50$, 100, 200, 300 mm) with a maximum to minimum size ratio of $L_{\max}/L_{\min} = 6$. These specimens are subject to uniaxial compression applying a constant stress rate of 0.02 MPa/s until the failure stress σ_f is reached. The specimens at varying sizes consistently exhibit relatively high stiffness despite notable fragmentation and spallation. For example, Figure 1(b) shows a highly damaged specimen (300mm) at 95% of peak load where the instantaneous Young's modulus of 2.7 GPa is close to the average value of 2.4 GPa of the specimen. The loading rate corresponds to an axial strain rate ranging from 7.4×10^{-5} to 9.5×10^{-5} s^{-1}. The elastic properties of the specimens appear largely unaffected by the sample size. This is supported by the ultrasonic pulse measurements, where p-wave velocities are consistent across all sizes at 1582 ± 40 m/s before loading. This consistency indicates that the smallest sample size used in this study ($L = 50$ mm) exceeds the representative elementary volume for the materials regarding quasistatic and dynamic elastic deformation. Furthermore, to assess the impact of sample geometry and dimension ratios on stress-strain relationships independently, uniaxial compression tests are conducted on six cylindrical specimens sized according to the ASTM standard testing method [39]. The details of these tests are provided in Appendix A.

The measured σ_f exhibits clear finite-size effects [orange error bars in Fig. 1(d)] which have been extensively studied experimentally [40,41]. The evolution of σ_f with increasing L could be approximated by power-law behaviors described by finite-size scaling theory [23–25]. This scaling law is characterized by power-law decay of σ_f until an asymptotic strength σ_∞ as L approaches infinity [23]:

$$\langle \sigma_f \rangle = \sigma_\infty (L/L_m)^{-1/\nu_{FS}} + \sigma_\infty, \tag{1}$$

where $\langle \sigma_f \rangle$ is the mean failure stress for the given size, L_m is a length scale associated with the microstructural disorder, and ν_{FS} is the finite-size exponent. In the current study, although we have 20 strength data of uniaxial compression, these are obtained across four sample sizes, so we could not fully constrain the confidence bounds of three parameters. Instead, we vary ν_{FS} from 0.5 to 4 and then estimate the other two parameters $\langle \sigma_f \rangle$ and L_m applying a fitting method of nonlinear least squares. Accordingly, theoretical prediction varying ν_{FS} at different values is derived alongside the size-dependent failure stress. We find that as ν_{FS} ranges between 1.1 and 2, theoretical predictions could closely align with the observed failure stress, as illustrated in Fig. 1(d).

C. Acoustic emission measurements

AEs are monitored during the failure process of 16 specimens [Fig. 2(a)]. For smaller specimens ($L = 50$ mm), the detection faces (orange cylinders) of two piezoelectric AE sensors [model: Nano30 from Physical Acoustics Corporation (PAC)] are directly coupled to the center positions on opposite free surfaces of the specimens. Conversely, the back of the sensors is subjected to pressure by steel springs, ensuring comparable sensor contact across all tests. For larger specimens ($L = 100$, 200, 300 mm), eight AE sensors are positioned diagonally to enhance spatial coverage following the same manner of installation.

Throughout the experiment, detected AEs, preamplified at 40 dB and bandpass filtered (between 10 kHz and 500 kHz), are recorded as voltage waveforms (blue squiggle) [Fig. 2(a)] via a PAC data acquisition system (DAQ) at a sampling rate of 1 MHz. P-wave first motion is defined as the area (unit: V/Hz, magenta shaded) beneath the voltage waveform starting from the p-wave onset (green dashed line) picked by Aikake information criterion (AIC) [42] until the first zero crossing of the voltage amplitude [43].

However, such first motion implicitly integrates the effects of sensor-sample contact, intrinsic sensor characteristics, cables, and analog/digital (A/D) converter across all failure tests. To eliminate these effects, AE sensors are absolutely calibrated between 1 kHz to 1 MHz following the methodology by Wu *et al.* [44,45], enabling the establishment of an explicit instrumental response (unit: V/pm) between the electrical output and vibration input. Ω (unit: pm/Hz) is defined as the ratio of the first motion to that instrumental response. Ω is referred to as the absolute amplitude of the low-frequency plateau of far-field components of seismic waves [46,47] and is directly proportional to the magnitude of seismic energies. Consequently, Ω represents the AE energies in this study, thus offering deep physical insights into seismic energy from failures of the materials under compression.

D. Data analysis

Our objective is to decipher the scale dependence of the temporal evolution of seismic features as materials approach failure, to which the distance is defined as

$$\Delta = 1 - \frac{\sigma}{\langle \sigma_f \rangle}, \tag{2}$$

where σ is the loading stress. As Δ progressively approaches zero, the system reaches the critical point, accompanied by intermittent AE events, of which two key acoustic attributes are examined across any given Δ interval: *1)* exponent ϵ depicting a probability distribution of AE energies; *2)* ASR or $d\Omega/d\Delta$ indicative of released AE energy over time. We focus on these acoustic attributes observable within the range of $10^{-3} < \Delta < 1$, beyond which the scarcity of AE events precludes a robust analysis. Note that the relationship between exponent ϵ in this study and b-value widely used in seismology, is $\epsilon = 1 + \frac{2}{3}b$ assuming the seismic magnitude M_w follows $M_w \propto \frac{2}{3} \log_{10} \Omega$ [48].
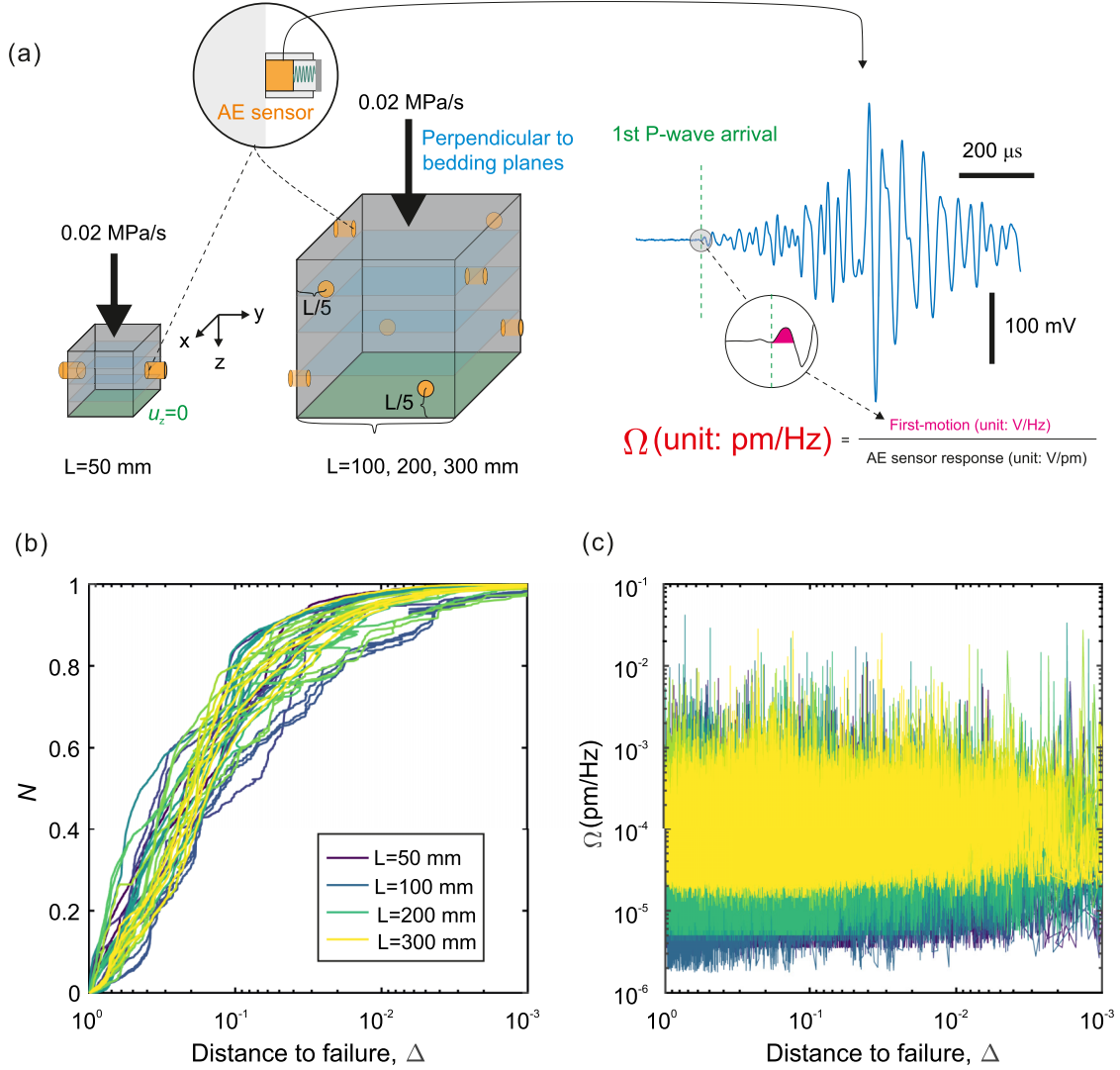
FIG. 2. Experimental setup and results visualization. (a) Schematic diagram of the experimental setup. Left: Samples of varying sizes under uniaxial compression with AE sensors (orange cylinder) installed on the vertical surfaces. Right: Measured voltage signal (blue squiggle) with p-wave onset (green dashed line). (Inset) P-wave first motion. (b) Normalized cumulative AE events, N, and (c) stacked surface vibrations, Ω, from all AE sensors across all failure tests against the distance to failure, $\Delta = 1 - \frac{\sigma}{\langle \sigma_f \rangle}$.

We consider AE energy Ω predominantly follows a power-law distribution whose probability density function (PDF) and complementary cumulative distribution function (CCDF) are expressed as [11,49]

$$P(\Omega) = \left(\frac{\epsilon - 1}{\Omega_c{}^{1-\epsilon}} \right) (\Omega)^{-\epsilon},$$

$$P(\Omega > \Omega_c) = 1 - \left(\frac{\Omega}{\Omega_c} \right)^{1-\epsilon}, \quad (3)$$

where Ω_c is the minimum cutoff of AE energy spectra beneath which power-law behaviors are masked by signal noise. The exponent ϵ is derived via maximum likelihood estimation (MLE) [50], fitting within the range from Ω_0 to maximum of Ω_i for each Δ subcatalog:

$$\epsilon = 1 + n \left(\sum_{i=1}^{n} \ln \frac{\Omega_i}{\Omega_0} \right)^{-1}, \quad (4)$$

where n is the total count of AE events with energies between Ω_0 and maximum of Ω_i. While implementing MLE for the exponent ϵ, null-hypothesis significance testing is performed to evaluate how likely AE energy distribution could have occurred under the null hypothesis of power-law distribution described by Eq. (4). Under the assumption that the null hypothesis is correct, the probability of power-law distribution at least as extreme as the AE energy distribution actually observed is obtained, or p-value. As Ω_0 incrementally increases within AE energy spectra, p-value is continuously evaluated for the goodness of fit of the power-law model described by Eq. (3). We determine Ω_0 as Ω_c once corresponding p-value continuously exceeds 0.05 in this study. As Ω_0 increases until the corresponding p-value continuously falls below 0.05, the maximum cutoff of Ω, termed as Ω_u, is detected. For AE energy spectra spanning from Ω_c and Ω_u, empirical CCDF follows a power-law decay characterized by the exponent ϵ. The calculation and result of p-value are detailed in Appendix B.
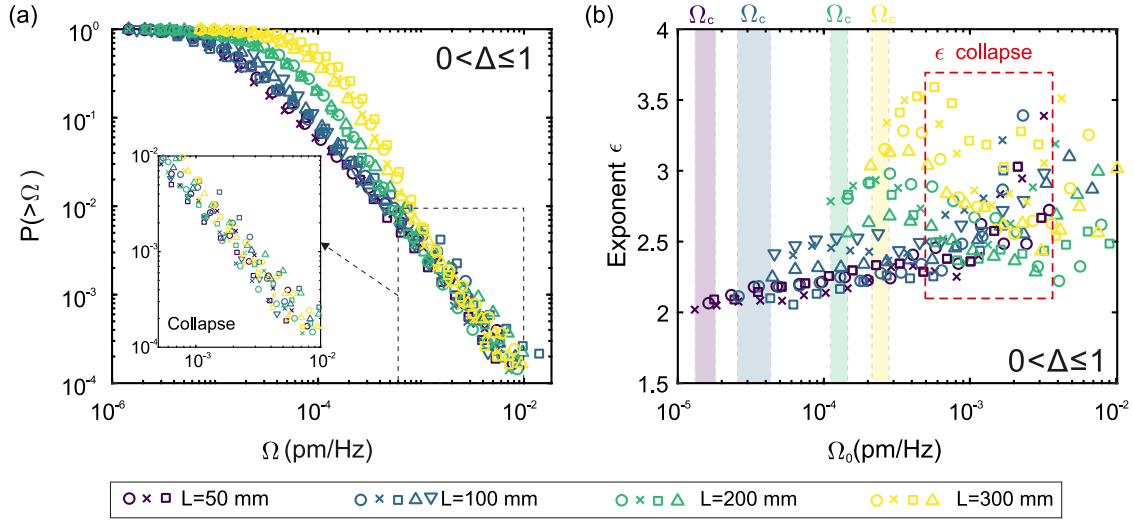
FIG. 3. Stress-integrated distribution of AE energies and maximum likelihood estimate (MLE) analysis on a statistical data set of 16 compressive tests. (a) Complementary cumulative distribution function (CCDF) of AE energies. (Inset) Data collapse of identical data in a rescaled plot. (b) Exponent ϵ from MLE whose p-values exceed 0.05. The calculation and results of p-values are detailed in Appendix B.

For critical failure, ASR or $d\Omega/d\Delta$ is defined as the product of AE activity rate $dN/d\Delta$ and average AE energy $d\Omega/dN$ or $\langle\Omega\rangle$ which typically follow power-law accelerations as $\Delta \to 0$:

$$\frac{d\Omega}{d\Delta} = \frac{d\Omega}{dN} \cdot \frac{dN}{d\Delta} = \langle\Omega\rangle \cdot \frac{dN}{d\Delta} \propto \Delta^{-(\alpha_{\langle\Omega\rangle}+\alpha_N)}, \quad (5)$$

$$\langle\Omega\rangle = \frac{d\Omega}{dN} \propto \Delta^{-\alpha_{\langle\Omega\rangle}}, \quad (6)$$

$$\frac{dN}{d\Delta} \propto \Delta^{-\alpha_N}, \quad (7)$$

where $dN/d\Delta$ indicates the frequency of AE event occurrences per unit Δ, $d\Omega/dN$ or $\langle\Omega\rangle$ is average AE energy per counts. N is the normalized cumulative number of AE events, $0 \leqslant N \leqslant 1$. $\alpha_{\langle\Omega\rangle}$ and α_N is the power-law exponent of $\langle\Omega\rangle$ and $dN/d\Delta$ against Δ, respectively. The case of $\alpha_{\langle\Omega\rangle}$ close to 0 indicates the lack of criticality. $\alpha_{\langle\Omega\rangle}$ and α_N are calculated through MLE methods [50]. To ensure statistical reliability in estimating ϵ and $d\Omega/d\Delta$, each test, at any given subcatalog of Δ, requires a minimum of 200 AE events. Furthermore, to maintain consistency across consecutive subcatalogs, an overlap of 20% of AE events is permitted.

III. RESULTS

The specimens at varying sizes exhibit consistent stiffness and high linearity up to 95% failure stress [Figs. 1(b) and 1(c)] while their strengths obey the expected finite-size scaling laws [Fig. 1(d)]. The temporal evolution of the normalized cumulative number of AE events N and AE energy Ω at various sample scales (purple to yellow) approaching failure are shown in Figs. 2(b) and 2(c), respectively. At each scale, N and Ω from AE sensors at different positions and repeated failure tests are shown following the same color. The temporal evolution of N overlaps well among different scales, which also apply to Ω. N rapidly increases to a range between 0.7

and 0.9 as Δ evolves close to 5×10^{-2}. Later, as $\Delta \to 0$, N slowly reaches 1. However, no clear trends are observed in the temporal evolution of Ω across all scales. For example, no significant rise of Ω is detected upon approaching failure. We find intermittency of AE events with high energies (e.g., $\Omega > 10^{-3}$ pm/Hz) separated by aftershocks. Moreover, high-energy events occur throughout the experiment, even at low axial stress (e.g., $\Delta \sim 10^{-1}$). As the sample size increases, the lower bound of AE energy spectra, Ω_c, progressively increases from approximately 5×10^{-6} to 2×10^{-5} pm/Hz. While the physical interpretation of Ω is ensured for all tests through AE sensor calibration [44,45], this sensitivity to sample size could be attributed to signal attenuation, i.e., the strong falloff of the radiated energies carried by elastic waves traveling more complex paths and significantly reflecting at defects in the larger specimens. Note that Ω show a slight decrease as Δ evolves from 2×10^{-3}. This is because intensive spalling behaviors cause partial fragments bonded with AE sensors to separate before catastrophic failure.

We show the empirical CCDFs of Ω of all AE events integrating the whole loading-to-failure cycle ($0 < \Delta \leqslant 1$) using Eq. (3) as the sample scales increased (purple to yellow) [Fig. 3(a)]. Such empirical CCDFs exhibit a clear power-law distribution whose exponent ϵ will be discussed in the following paragraph. A clear system-size dependence exists on the minimum cutoff of AE energy spectra, Ω_c, which share similarity with the lower bound of Ω spectra [Fig. 2(c)]. For energies above Ω_c but below intermediate energies (e.g., 5×10^{-4} pm/Hz), the power-law relationship is steeper for large samples, indicating a higher power-law exponent. Such system-size drift reflects the characteristic scale of the fracturing events as $\Omega \propto r^3$ assuming r is the radius of a penny-shaped elastic crack [51–53], and thus larger samples tend to generate a higher portion of small microcracks. For energies above intermediate energies (e.g., 5×10^{-4} pm/Hz), Ω at all scales collapses as Δ varies by more than one order of magnitude [Inset of Fig. 3(a)]. This indicates that Ω at high energies is only weakly scale-dependent. This might reveal
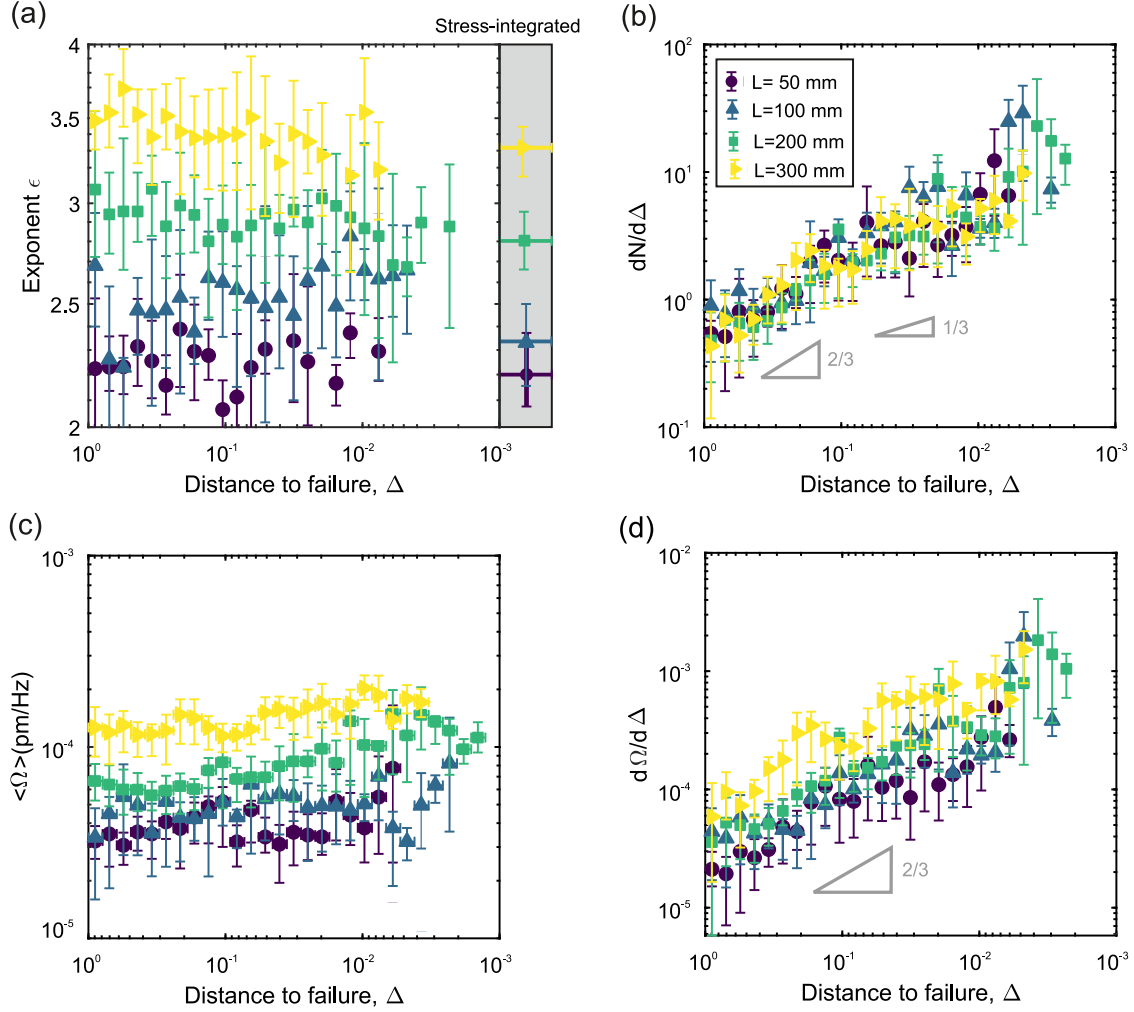
FIG. 4. Temporal evolution of acoustic attributes with distances to failures for all sample sizes (50 to 300 mm, purple to yellow). Each color corresponds to the averaged features with 95% confidence from all AE sensors across failure tests at the same size. The legend is consistent across all panels. (a) Exponent ϵ that describes a power-law distribution of AE energies. Grey shaded: stress-integrated ϵ from Fig. 3(b). (b) AE activity rate $dN/d\Delta$, (c) average AE energy $\langle\Omega\rangle$, and (d) accelerated seismic release (ASR) $d\Omega/d\Delta$. Grey triangles indicate the reference exponent that depicts the power-law populations.

that upon approaching failure, some large macroscopic fractures, which contribute to significant loss of system stability, share a similar distribution of geometry size since the sample size is limited under experimental conditions.

We then implement MLE methods detailed in Sec. II D to stress-integrated CCDFs of Ω [Fig. 3(a)] and calculate the exponent ϵ distributed along the Ω spectra [Fig. 3(b)]. We only show the exponent ϵ whose p-value exceeds 0.05 from hypothesis tests where methods and results are detailed in Appendix B. As the sample size increases, there is clear scale dependence of the exponent ϵ (2.2 ± 0.1 to 3.3 ± 0.2) below intermediate energies of 5×10^{-4} pm/Hz. Above intermediate energies, the exponent ϵ collapses to around 2.6 ± 0.3 until energies of approximately 5×10^{-3} pm/Hz. When energies are greater than 5×10^{-3} pm/Hz, there is a divergence of the exponent ϵ because of insufficient AE events with extremely high energies. Note that the calculated ϵ is relatively high, e.g., above 2, which is larger than previous observations that ϵ is generally less than 2 [28]. We argue these differences might be attributed to the absolute calibration applied

to our AE data and to the microstructural heterogeneities of the coal material, which is also observed at the field-scale seismicity [54–56]. To eliminate the attenuation effect from the calculation of the higher exponent ϵ [57–59], we quantify the acoustic energy loss due to attenuation in Appendix C and validate ϵ is calculated only from the power-law portion (or linear portion in log-log space) of the AE energy population in Appendix D.

IV. DISCUSSION

A. Does the distribution of AE energies exhibit scale dependence?

We examine the temporal evolution of acoustic characteristics with distances to failures, Δ, across varying sample sizes [Fig. 4]. The exponent ϵ and accelerated seismic release (ASR) $d\Omega/d\Delta$ are derived via methodologies outlined in Sec. II D as Δ diminishes to zero over 30 logarithmically spaced subcatalogs within the range of $10^{-3} < \Delta < 1$. Notably, data are not available as the system approaches

catastrophic failure, especially within the $10^{-3} < \Delta < 5 \times 10^{-3}$ interval. This occurs due to the count of AE events in these subcatalogs significantly falling below 200, a threshold set in Sec. II D. The color coding represents the averaged acoustic features from all AE sensors across failure tests at the same size. The error bars signify the ranges expected with 95% confidence. Note that our efforts to quantify the exponent ϵ utilizing the AE energy spectra between intermediate and extremely high energies are hindered by a very limited number of AE events with high energies.

Within each Δ subcatalog, the exponent ϵ is calculated through the implementation of MLE methods to CCDFs of Ω dataset, confined between the minimum cutoff Ω_c and intermediate energies (e.g., 5×10^{-4} pm/Hz). The CCDFs of Ω recorded at a single AE sensor from the smallest (50 mm) and largest (300 mm) sample sizes are provided in Appendix D, as an example. At any stress level, with the ratio of the sample size increasing from 1 to 6, the stress-dependent ϵ exhibits an overall increase of approximately 1.2 ± 0.2 [left panel in Fig. 4(a)]. The stress-integrated ϵ from all sample sizes is added to the right panel, showing a comparable span as ϵ at any stress level. This scale-dependent phenomenon in stress-dependent and stress-integrated ϵ indicates that large-scale samples are susceptible to generating a larger portion of small microcracks in brittle materials around pre-existing large fractures.

B. Would stress-dependent ϵ decrease as the system approaches failures?

At any given sample size, as Δ diminishes to zero, the exponent ϵ does not exhibit clear trends [Fig. 4(a)] as AE energy spectra tend to collapse following a similar power-law distribution [Fig. 8 from Appendix D]. Yet, the exponent ϵ is typically suggested to decrease upon approaching failure as microcracks propagate and coalesce into larger cracks [12,16,32]. Here, we argue that pre-existing fracture systems observed in studied materials [Fig. 1(a)] could account for observed ϵ behaviors. As external loading increases, even at a low-stress level, failure at these large-scale heterogeneities could be reached before the intact matrix, leading to a release of accumulated strain energies accompanied by intermittent audible bursts. The local stress is intermittently transferred to the surrounding matrix, resulting in progressive stress concentration at a decreasing number of force chains that are far from spallation, bear external loading, and prevent structural collapse [Fig. 1(b)]. This is supported by consistent stiffness and high linearity before close to failure up to 95% failure stress [Fig. 1(c)]. The absence of extremely large events near failure further confirms this [Fig. 1(d)]. The failure process is relatively progressive in contrast with intact brittle materials such as intact compressed granite [12]; however, ϵ evolution shares inherent similarities with that in granite containing single pre-cut notch loaded in compression [36]. Accordingly, the probability distribution of radiated AE energies almost maintains its shape, and the exponent ϵ is almost stationary as the material approaches failure. We further confirm such stationary behaviors of the exponent ϵ using hypothesis testing in Appendix E.

C. How does accelerated seismic release (ASR) change upon approaching failure?

For all sample sizes, AE activity rate $dN/d\Delta$ exhibits a significant positive dependence on the distances to failures, Δ, as $dN/d\Delta \propto \Delta^{-\alpha_N}$ (also known as time-reversed Omori's law [60]) [Fig. 4(b)]. In particular, the exponent α_N behaves independently of the sample size as the size ratio varies until 6, which resembles the α_N behaviors in concretes with the size ratio ranges until 4 [32]. Among all sample sizes, $dN/d\Delta$ increases faster in the earlier stage (e.g., $\Delta > 10^{-1}$) than in the case of approaching failures. This indicates a transition beyond which the behavior of $dN/d\Delta$ with respect to Δ significantly shifts. We determine such transition points via segmented regression (detailed in Appendix F) for all sample sizes as Δ equal 0.18, 0.18, 0.11, and 0.13, respectively. For Δ below these transition points, α_N is estimated as 0.66 ± 0.1. The measured exponent α_N is comparable to measurements in other heterogeneous brittle solids. For example, sandstone (around 1 from [61]), concrete (0.66 ± 0.05 from [32]), coal (0.66 to 0.75 from [28]), packed cellular solids (0.73 ± 0.03 from [34]), intact granite (0.96 ± 0.06 from [36]). However, the average AE energy $\langle \Omega \rangle$ tends to be stationary as $\Delta > 10^{-1}$ [Fig. 4(c)]. As a result, ASR $d\Omega/d\Delta$ share a similar critical exponent with AE activity rate $dN/d\Delta$ [Figs. 4(b) and 4(d)].

When the material progressively approaches failure (e.g., $\Delta < 10^{-1}$), microcracks begin to coalesce at the specimen-scale, drawing upon the structure of the fracture networks that play a key role. The exponent α_N decreases to approximately 0.33 ± 0.1 [Fig. 4(b)]. We have confirmed the utilized AE systems did not reach saturation nor missed registering AE events during this period. Previous experimental studies show that α_N could decrease from 0.75 in more homogeneous, less porous materials to 0.66 in heterogeneous and porous materials [28]. Large structural inhomogeneities from a single fault cause α_N to fall from 0.96 to 0.85 [36]. The falloff in α_N or the suppressed critical failure could be explained by the fact that cracking primarily nucleates at the heterogeneous element near fracture systems instead of generating a significant number of new microcracks within the relatively intact matrix.

In our tests, the average AE energy $\langle \Omega \rangle$ exhibits a slow increase as $\Delta < 10^{-1}$ [Fig. 4(c)]. This could be partially attributed to the fact that upon approaching failure, the effective area of force chains that bear external loading progressively decreases such that stress-induced damage is more localized with higher AE energy released. The macroscopic coalescence of fracture networks and generated cracks could also account for the rise in observed AE energy. Increased $\langle \Omega \rangle$ highlights differences between AE activity rate $dN/d\Delta$ and ASR $d\Omega/d\Delta$ [Figs. 4(b) and 4(d)]. No clear transitions are observed in $d\Omega/d\Delta$ as the proximity to the failure decreases from 1 to 0. We calculate the corresponding power-law exponent of $d\Omega/d\Delta$ as 0.77 ± 0.05 for all sample sizes. Thus, ASRs exhibit independence in the sample size and are general without criticality.

V. CONCLUSION

Based on laboratory compressive experiments, we investigate the size effect and stress dependence on foreshock activities preceding damage localization in fractured brittle

materials. We find seismic precursors such as AE energy distribution and ASR generally follow the power-law distribution. The size effect of AE energy distribution varies along the spectrum range of radiated AE energy. At low energy, fractured material with a larger sample size tends to produce a larger portion of small microcracks. As the studied spectra increase towards infinity, the size effect almost disappears such that fractured media at the investigated range of sample size share a similar distribution of AE energies. Moreover, our work confirms that in the existence of fracture systems, as a set of large-scale structural heterogeneities, the temporal evolution of AE energy population is relatively stationary without a critical point and exhibits little fluctuations on the power-law exponent. This phenomenon significantly differs from the extensive observations in relatively intact materials [32]. Nevertheless, our results are close to the AE statistics of a rock containing a single large pre-existing fracture [36]. AE activity rate is found to be independent of sample size, which is also confirmed in concrete [32]. However, regarding a highly fractured material, the AE activity rate shows notable time dependency. During the early stages of loading at large distances to failure, the exponent is approximately 2/3, also found in many materials [16,28,32,34,62]. However, close to failure, the AE activity rate increases more slowly, and the exponent is close to 1/3. ASR exhibits generality rather than critical failure.

We suppose the well-developed fracture systems may account for observed AE statistics. Interconnected fractures spanning multiple geometry scales might induce a highly heterogeneous stress field inside the brittle solids. As external loading stress escalates, failure criteria around these strong heterogeneities may be met sooner than in the intact matrix, even at low-stress levels. This results in the intermittent release and redistribution of local stress and strain energy, leading to the birth of many AE events with sufficient energies in the early stage of the failure, while there are much fewer AE events with low energies in the intact material with relatively homogeneous microstructure. This might explain why the AE energy distribution is stationary and the AE activity rate increases slower upon approaching failure. Our results, elucidating the size effect and stress dependence on AEs in fractured rocks, have important implications for precursor studies in many natural hazards and engineering instability.

ACKNOWLEDGMENTS

APPENDIX A: UNIAXIAL COMPRESSIVE BEHAVIORS OF CYLINDRICAL SAMPLES

To preclude the effect of the sample geometry and dimension ratio on compressive test results, six supplemental tests are performed on cylinders (diameter: 50 mm, length: 100 mm) sampled from the identical block following the same preparation and loading procedures as cubic specimens.
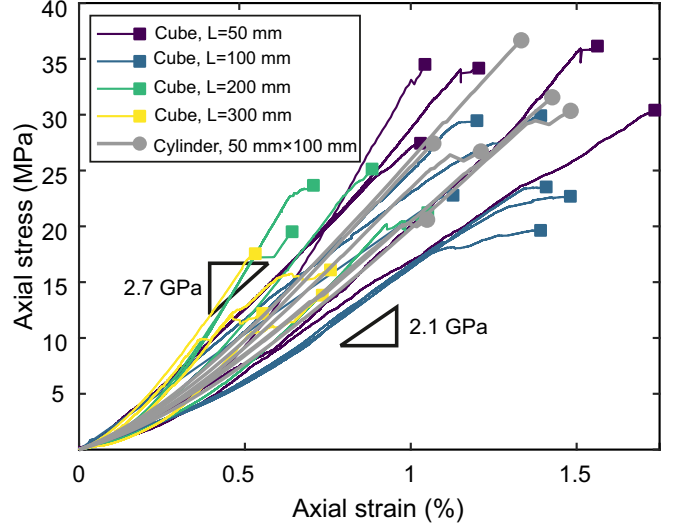

FIG. 5. Stress-strain results of 20 cubic (50, 100, 200, 300 mm) and six cylindrical (diameter: 50 mm, length: 100 mm) specimens subject to uniaxial compression.

Loading faces of cubic and cylindrical specimens are ground flat with an uncertainty of ± 0.1 mm.

Measured stress-strain results are shown in Fig. 5 for cubic (purple to yellow) and cylindrical (grey) specimens. We find the failure stress of cylinders (grey) approximately located at the measured range from cubes at 50 (purple) and 100 (blue) mm. Furthermore, the deformability of cylinders (grey) shares similarities with cube specimens of 50 (purple) and 100 (blue) mm. Therefore, we conclude that the cubic geometry and a dimension ratio of 1:1:1 from the main experiments have a minimal effect on the stress-strain results and thus accompanying AE behaviors.

APPENDIX B: HYPOTHESIS TEST FOR EXPONENT ϵ IN MAXIMUM LIKELIHOOD ESTIMATION

When performing maximum likelihood estimation (MLE) on ϵ values, we must examine the fitting bounds $[\Omega_0, \max(\Omega)]$, outside which the AE energies Ω could deviate from the reference power-law distribution described by Eq. (3). To test the null hypothesis that the power-law model cannot be rejected at a high confidence level, we adopt the Kolmogorov-Smirnov (KS) statistic, which measures the maximum distance between the empirical and theoretical CCDF [Eq. (3)] of AE energies Ω.

For Ω spectra at any Δ interval, we logarithmically split such spectra into 100 consecutive bins bounded by $[\min(\Omega), \max(\Omega)]$. Then we incrementally increased Ω_0 from $\min(\Omega)$ to $\max(\Omega)$. At each fitting range $[\Omega_0, \max(\Omega)]$, MLE method is performed to estimate the exponent ϵ using Eq. (4). Using the estimated ϵ, 1000 synthetic datasets of AE energies Ω_n, independently and identically distributed between $[\min(\Omega), \max(\Omega)]$, is generated from the theoretical CCDF described by Eq. (3). For each synthetic dataset, its KS statistic D is calculated against the theoretical CCDF using maximum absolute difference

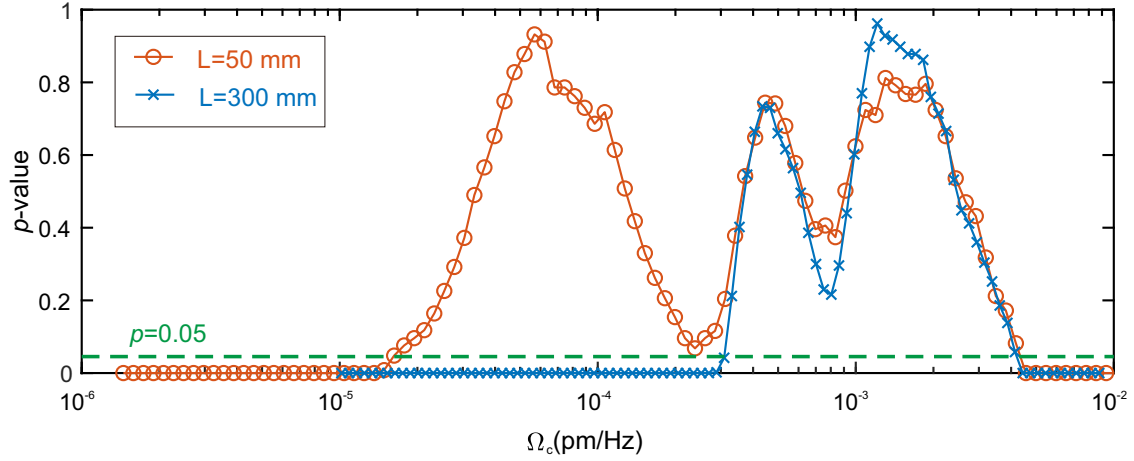$$D = \max |\text{CCDF}(\Omega_n) - \text{CCDF}(\Omega)|. \tag{B1}$$

FIG. 6. Results of p-value for the goodness-of-fit of the AE energy distribution. High p-value indicates that the null hypothesis of a power-law behavior cannot be rejected.

The p-value is the fraction of synthetic datasets whose KS statistic is greater than that calculated from the actual data ($D > 0$). Here p-values calculated from AE energies recorded at a single AE sensor from the smallest (50 mm) and largest (300 mm) sample size are shown in Fig. 6 as an example. We consider the null hypothesis of power-law distribution of AE energies as true until p-value reaches 0.05 (green dashed line) as Ω_0 increased. $p \geqslant 0.05$ also helps to determine Ω_c below which Ω spectra is truncated and deviated from the power-law distribution.

APPENDIX C: CHARACTERIZATION OF SEISMIC ATTENUATION

To quantify the acoustic energy loss due to seismic attenuation, we have evaluated the quality factor Q of the studied material. Q is a dimensionless quantity representing the ratio of acoustic energy to energy lost per cycle [2]. Larger values of Q indicate less seismic attenuation. We follow the spectral ratio method [63–65] and ultrasonic monitoring of pulse transmission [66] is performed on coal materials studied, and a reference material, aluminum, with identical geometry to exclude frequency-independent geometrical factor. Aluminum is used due to its extremely low attenuation (i.e., $Q = 1.5 \times 10^5$ by Zemanek and Rudnick [67]) relative to coal materials. Windowed waveforms of direct waves centered on the p-wave first arrival are shown in the frequency domain from five coal (blue to yellow) and one aluminum (gray) specimens [Fig. 7(a)]. For each specimen, twenty repeated ultrasonic surveys are performed. We find that acoustic energy in aluminum is significantly higher than in coal specimens, where acoustic energy can hardly be transmitted once the studied frequency exceeds 200 kHz. Thus, we determine a frequency range of 30 kHz to 200 kHz for calculating Q.
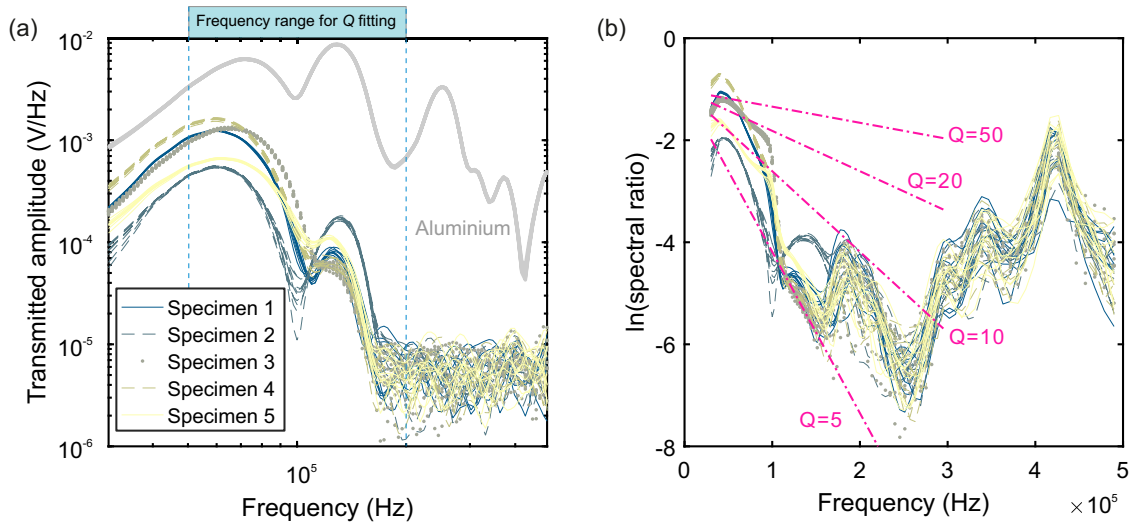

FIG. 7. (a) Direct waves centered on the p-wave first arrival in the frequency domain from five coal and one aluminum specimen. For each specimen, twenty repeated ultrasonic surveys are performed. (b) Natural logarithm of the ratio of coal to aluminum in the frequency domain. Red dashed lines represent the quality factor $Q = 5$, 10, 20, and 50.
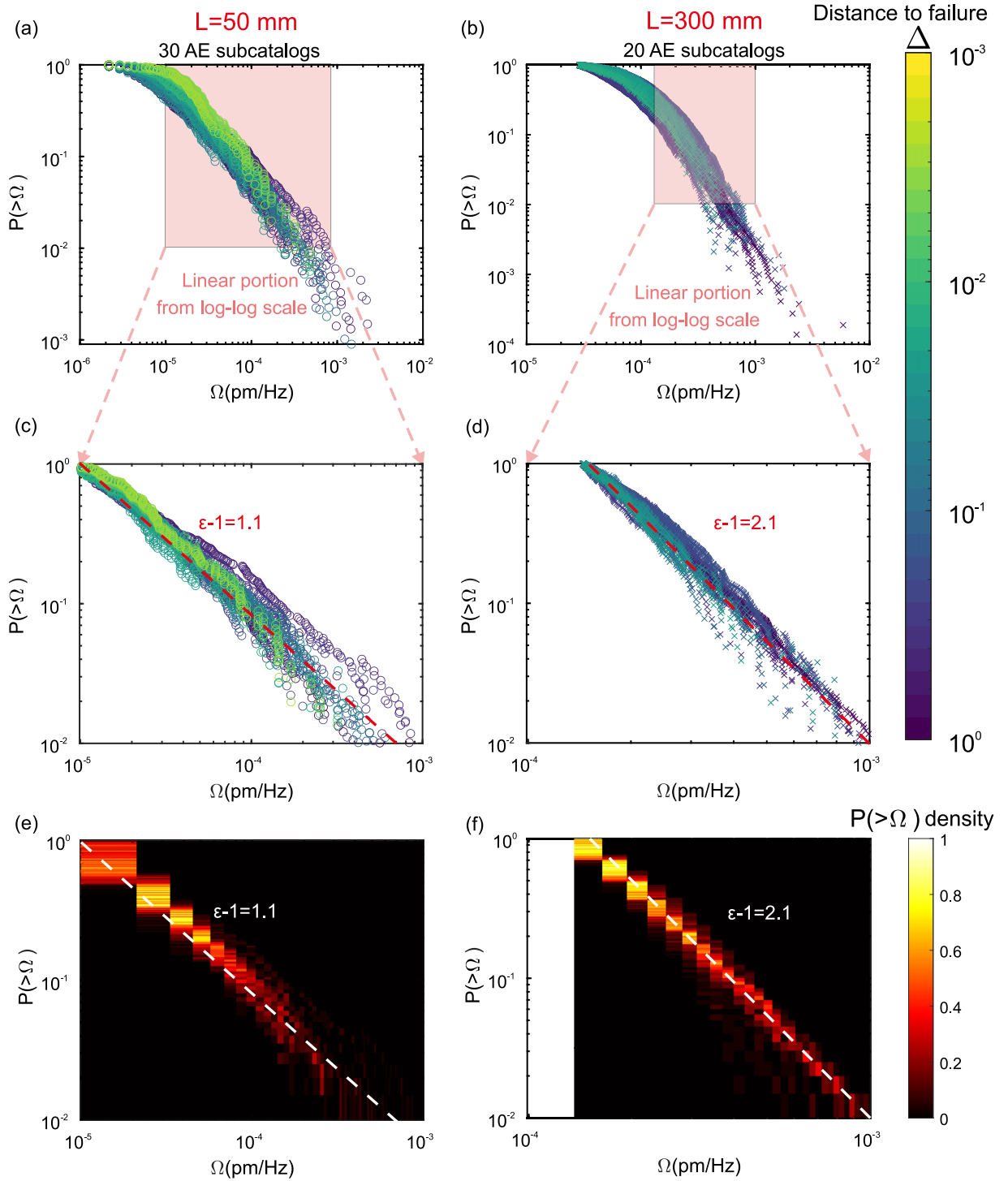
FIG. 8. Stress-dependent distribution of AE energies recorded at a single AE sensor from the smallest (50 mm) and largest (300 mm) sample sizes. (c) and (d) are the insets of (a) and (b) considering power-law fitting, respectively. Each curve corresponds to AE energy spectra at varying distances to failure: the purple curve is farthest, and the yellow curve is closest to failure. (e) and (f) are the density maps of (c) and (d) respectively.

The amplitude (A) of plane elastic body waves at the specific frequency for the aluminum (subscript 1) and coal specimens (subscript 2) can be expressed as

$$A_1(f) = G_1(x)e^{-\frac{\pi f x}{Q_1 v_1}} e^{i(2\pi f - k_1 x)}, \quad \text{(C1)}$$

$$A_2(f) = G_2(x)e^{-\frac{\pi f x}{Q_2 v_2}} e^{i(2\pi f - k_2 x)}, \quad \text{(C2)}$$

where f and k are the frequency and wave number of the received waveforms, v is the wave velocity (longitudinal waves are considered here), x is the distance between the ultrasonic transmitter and receiver ($x = 100$ mm), and $G(x)$ is a frequency-independent geometrical factor. The natural logarithm of the spectral ratio of transmitted amplitude for

coal specimens (A_2) to aluminum (A_1) is given as

$$\ln\left(\frac{A_2}{A_1}\right) \propto \left(\frac{1}{Q_1 v_1} - \frac{1}{Q_2 v_2}\right)\pi x f \qquad (C3)$$

and is shown in Fig. 7(b). Since Q_1 (aluminium) is extremely high compared to Q_2 (coal) so that the term $1/Q_1 v_1$ is ignored. Then Eq. (C3) can be simplified as

$$\ln\left(\frac{A_2}{A_1}\right) \propto -\frac{\pi x}{Q_2 v_2} f. \qquad (C4)$$

After evaluating the slope ($-\pi f x/Q_2 v_2$) using nonlinear least squares, we find that Q ranges between 5 and 10 for the studied material as shown in Fig. 7(b). The calculated Q factor is similar to those found in previous laboratory studies on Navajo sandstone ($\sim$7.3), Boise sandstone ($\sim$6.9), and Berea sandstone ($\sim$20) [63]. We can further estimate the amplitude attenuation coefficient α for our laboratory setting:

$$\alpha = e^{-\frac{\pi f x}{Q v}}, \qquad (C5)$$

where x is the distance from the AE source to sensors. Since the AE localization is not available in this study, we assume most AE sources concentrate at the specimen center for the maximum size (300 mm), i.e., $x = 162$ mm. Given that Q is 10, f is 50 kHz, and v is 1582 m/s, α is estimated to be around 24.7%, i.e., the amplitude detected at the AE sensor is 24.7% of the amplitude if the sensor is immediately at the source. This coefficient α is relatively large on a log-scale and we can conclude that the effect of the attenuation is not very significant. Thus, the seismic attenuation is not likely to significantly affect the right side of the AE event size distribution. Nevertheless, future modeling of the attenuation effect in the current study with AE localization would provide us with more insights.

APPENDIX D: STRESS-DEPENDENT DISTRIBUTION OF AE ENERGIES

We present the raw AE energy distributions recorded at a single AE sensor from the smallest (50 mm) and largest (300 mm) specimens in Figs. 8(a) and 8(b), respectively, as an example. Each curve corresponds to AE energy spectra at varying distances to failure: the purple curve is farthest, and the yellow curve is closest to failure. We observe that at the two sides of raw AE energy distributions, AE energies deviate from the power-law distribution when AE energies are above around 1×10^{-3} pm/Hz or below 1×10^{-5} pm/Hz. Such deviation requires us to determine a power-law portion (or linear portion in log-log space) for estimating the power-law exponent ϵ.

First, the left boundary of the power-law portion of AE energies, or AE magnitude of completeness, is determined using a p-value $\geqslant 0.05$ (green dashed line) in the left side in Fig. 6. A high p-value indicates that the null hypothesis of a power-law behavior cannot be rejected. On the other hand, we derive the right boundary for power-law fitting as the 99th percentile of AE energies [68]. This results in a right-side cutoff AE energy of around 1×10^{-3} pm/Hz [on right side of the pink box in Figs. 8(a) and 8(b)], which is much more conservative compared to AE energy of around 4×10^{-3} pm/Hz calculated from p-value $\geqslant 0.05$ [right side in Fig. 6].

Consequently, we determine regions exhibiting significant power-law distribution [pink box in Figs. 8(a) and 8(b)], shown in detail in Figs. 8(c) and 8(d). We find that such AE energy spectra are relatively 'linear' in the log-log space, especially with the further validation of their density maps as shown in Figs. 8(e) and 8(f), leading to a proper estimation of power-law exponent ϵ. Therefore, we could eliminate the attenuation effect from the calculation of the power-law exponent ϵ.

APPENDIX E: HYPOTHESIS TEST FOR STATIONARY BEHAVIORS OF EXPONENT ϵ

As observed in Fig. 4(a), the power-law exponent ϵ is almost stationary as the material approaches failure. To further confirm this, hypothesis tests are performed on whether the correlation coefficient α_ϵ between Δ and ϵ significantly differs from 0. The null hypothesis is that α_ϵ equals zero. As the sample size increases, α_ϵ is calculated as -0.23, -0.06, 0.07, 0.10 with corresponding p-value of 0.07, 0.50, 0.39, 0.21, respectively. Thus, the null hypothesis is accepted for all studied sample sizes at the 5% significance level. Note that α_ϵ for a small size (50 mm) is significantly larger than other sizes, possibly resulting from the fact that the small sample exhibits higher homogeneity and integrity.

APPENDIX F: TRANSITION BETWEEN THE FAST- AND SLOW-GROWING REGION OF AE ACTIVITY RATE $dN/d\Delta$

As observed in Fig. 4(b), there appear to exist transitions between the fast- and slow-growing region of AE activity rate $dN/d\Delta$. These transitions are identified using a statistical approach known as segmented regression [69]. This technique allows for the detection of one or more breakpoints which effectively partition the dataset presented in Fig. 4(b) into segments. Within each segment, linear models are fitted
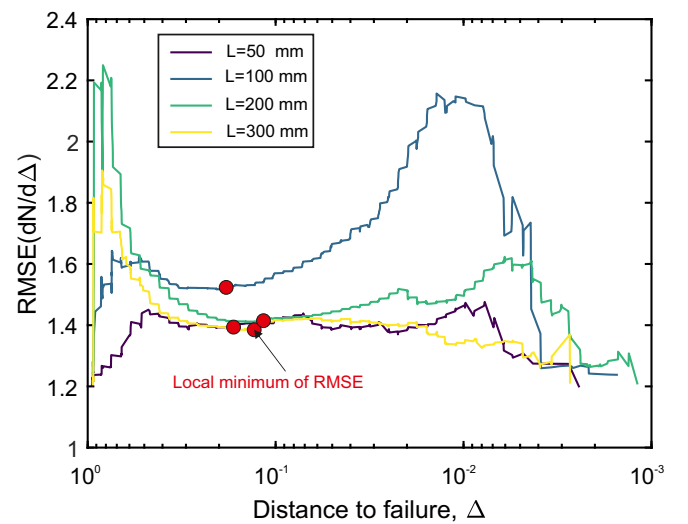

FIG. 9. Root mean square error (RMSE) of AE activity rate $dN/d\Delta$ for all sample sizes while the transition point moves towards failure. The local minimum (red circles) indicates the optimum transition point that splits the fast- and slow-growing region of AE activity rate $dN/d\Delta$.

independently. The determination of the optimal breakpoint is achieved through iterative procedures, during which various candidate breakpoints are assessed to minimize an error criterion. In this study, the sum of root mean squared errors (RMSE) across the different segments serves as the error (Fig. 9). The locations yielding the minimum RMSE are selected as the transition points for all sample sizes, with Δ equals 0.18, 0.18, 0.11, and 0.13, respectively.

[1] G. C. P. King, R. S. Stein, and J. Lin, Static stress changes and the triggering of earthquakes, Bull. Seismol. Soc. Am. **84**, 935 (1994).

[2] P. M. Shearer, *Introduction to Seismology* (Cambridge University Press, Cambridge, 2009).

[3] G. B. Crosta and F. Agliardi, Failure forecast for large rock slides by surface displacement measurements, Can. Geotech. J. **40**, 176 (2003).

[4] A. F. Bell, M. Naylor, and I. G. Main, The limits of predictability of volcanic eruptions from accelerating rates of earthquakes, Geophys. J. Int. **194**, 1541 (2013).

[5] G. Kwiatek and Y. Ben-Zion, Assessment of P and S wave energy radiated from very small shear-tensile seismic events in a deep South African mine, J. Geophys. Res.: Solid Earth **118**, 3630 (2013).

[6] R. M. Holt, E. Fjær, J. F. Stenebråten, and O.-M. Nes, Brittleness of shales: Relevance to borehole collapse and hydraulic fracturing, J. Pet. Sci. Eng. **131**, 200 (2015).

[7] Z. P. Bažant, F. Lin, and H. Lippmann, Fracture energy release and size effect in borehole breakout, Int. J. Numer. Anal. Methods Geomech. **17**, 1 (1993).

[8] S. C. Cowin, *Bone Mechanics Handbook* (CRC Press, Boca Raton, FL, 2001), p. 968.

[9] C. U. Grosse and M. Ohtsu, *Acoustic Emission Testing* (Springer Science & Business Media, Berlin, 2008).

[10] D. Lockner, The role of acoustic emission in the study of rock fracture, Int. J. Rock Mech. Min. Sci. Geomech. Abstr. **30**, 883 (1993).

[11] I. Main, Statistical physics, seismogenesis, and seismic hazard, Rev. Geophys. **34**, 433 (1996).

[12] C. H. Scholz, The frequency-magnitude relation of microfracturing in rock and its relation to earthquakes, Bull. Seismol. Soc. Am. **58**, 399 (1968).

[13] P. Diodati, F. Marchesoni, and S. Piazza, Acoustic emission from volcanic rocks: An example of self-organized criticality, Phys. Rev. Lett. **67**, 2239 (1991).

[14] D. Sornette, Power laws without parameter tuning: An alternative to self-organized criticality, Phys. Rev. Lett. **72**, 2306 (1994).

[15] Y. Ben-Zion and V. Lyakhovsky, Accelerated seismic release and related aspects of seismicity patterns on earthquake faults, Pure Appl. Geophys. **159**, 2385 (2002).

[16] G. F. Nataf, P. O. Castillo-Villa, J. Baró, X. Illa, E. Vives, A. Planes, and E. K. H. Salje, Avalanches in compressed porous SiO_2-based materials, Phys. Rev. E **90**, 022405 (2014).

[17] J. Baró, Á. Corral, X. Illa, A. Planes, E. K. H. Salje, W. Schranz, D. E. Soto-Parra, and E. Vives, Statistical similarity between the compression of a porous material and earthquakes, Phys. Rev. Lett. **110**, 088702 (2013).

[18] D. Sornette, *Critical Phenomena in Natural Sciences: Chaos, Fractals, Selforganization and Disorder: Concepts and Tools* (Springer Science & Business Media, Berlin, 2006).

[19] Z. P. Bažant and L. Cedolin, *Stability of Structures: Elastic, Inelastic, Fracture and Damage Theories* (World Scientific, Singapore, 2010).

[20] C.-C. Vu, J. Weiss, O. Plé, D. Amitrano, and D. Vandembroucq, Revisiting statistical size effects on compressive failure of heterogeneous materials, with a special focus on concrete, J. Mech. Phys. Solids **121**, 47 (2018).

[21] W. Weibull, A statistical distribution function of wide applicability, J. Appl. Mech. **18**, 293 (1951).

[22] E. J. Gumbel, *Statistics of Extremes* (Columbia University Press, New York, 1958).

[23] J. Weiss, L. Girard, F. Gimbert, D. Amitrano, and D. Vandembroucq, (Finite) statistical size effects on compressive strength, Proc. Natl. Acad. Sci. **111**, 6231 (2014).

[24] M. Sahimi and J. D. Goddard, Elastic percolation models for cohesive mechanical failure in heterogeneous systems, Phys. Rev. B **33**, 7848 (1986).

[25] M. Sahimi, *Heterogeneous Materials: Nonlinear and Breakdown Properties and Atomistic Modeling* (Springer, 2003), Vol. 2, p. 638.

[26] J. Vasseur, F. B. Wadsworth, Y. Lavallée, A. F. Bell, I. G. Main, and D. B. Dingwell, Heterogeneity: The key to failure forecasting, Sci. Rep. **5**, 13259 (2015).

[27] E. K. H. Salje, A. Saxena, and A. Planes, *Avalanches in Functional Materials and Geophysics*, 1st ed. (Springer, Berlin, 2017), p. 298.

[28] Y. Xu, A. G. Borrego, A. Planes, X. Ding, and E. Vives, Criticality in failure under compression: Acoustic emission study of coal and charcoal with different microstructures, Phys. Rev. E **99**, 033001 (2019).

[29] X. Jiang, H. Liu, I. G. Main, and E. K. H. Salje, Predicting mining collapse: Superjerks and the appearance of record-breaking events in coal as collapse precursors, Phys. Rev. E **96**, 023004 (2017).

[30] A. Cartwright-Taylor, M.-D. Mangriotis, I. G. Main, I. B. Butler, F. Fusseis, M. Ling, E. Andò, A. Curtis, A. F. Bell, A. Crippen, R. E. Rizzo, S. Marti, D. D. V. Leung, and O. V. Magdysyuk, Seismic events miss important kinematically governed grain scale mechanisms during shear failure of porous rock, Nat. Commun. **13**, 6169 (2022).

[31] D. Soto-Parra, E. Vives, M. E. Botello-Zubiate, J. A. Matutes-Aquino, and A. Planes, Acoustic emission avalanches during compression of granular manganites, Appl. Phys. Lett. **112**, 251906 (2018).

[32] C.-C. Vu, D. Amitrano, O. Plé, and J. Weiss, Compressive failure as a critical transition: Experimental evidence and mapping onto the universality class of depinning, Phys. Rev. Lett. **122**, 015502 (2019).

[33] T. Mäkinen, A. Miksic, M. Ovaska, and M. J. Alava, Avalanches in wood compression, Phys. Rev. Lett. **115**, 055501 (2015).

[34] A. Mayya, E. Berthier, and L. Ponson, How criticality meets bifurcation in compressive failure of disordered solids, Phys. Rev. X **13**, 041014 (2023).

[35] T. H. W. Goebel, G. Kwiatek, T. W. Becker, E. E. Brodsky, and G. Dresen, What allows seismic events to grow big? Insights from b-value and fault roughness analysis in laboratory stick-slip experiments, Geology **45**, 815 (2017).

[36] A. Patton, T. Goebel, G. Kwiatek, and J. Davidsen, Large-scale heterogeneities can alter the characteristics of compressive failure and accelerated seismic release, Phys. Rev. E **108**, 014131 (2023).

[37] A. Cartwright-Taylor, I. G. Main, I. B. Butler, F. Fusseis, M. Flynn, and A. King, Catastrophic failure: How and when? Insights from 4-D in situ x-ray microtomography, J. Geophys. Res.: Solid Earth **125**, e2020JB019642 (2020).

[38] E. Bonnet, O. Bour, N. E. Odling, P. Davy, I. Main, P. Cowie, and B. Berkowitz, Scaling of fracture systems in geological media, Rev. Geophys. **39**, 347 (2001).

[39] ASTM D7012-04, *Standard Test Method for Compressive Strength and Elastic Moduli of Intact Rock Core Specimens under Varying States of Stress and Temperatures* (ASTM International, West Conshohocken, Pennsylvania, 2017).

[40] E. Hoek and E. T. Brown, Practical estimates of rock mass strength, Int. J. Rock Mech. Min. Sci. **34**, 1165 (1997).

[41] F. Gao, X. Peng, G. Yuan, and W. Liu, Laboratory investigation of scale effects in bursting failure of quasi-brittle materials, Int. J. Rock Mech. Min. Sci. **171**, 105579 (2023).

[42] H. Akaike, A new look at the statistical model identification, IEEE Trans. Autom. Control **19**, 716 (1974).

[43] G. Kwiatek, P. Martínez-Garzón, and M. Bohnhoff, HybridMT: A MATLAB/shell environment package for seismic moment tensor inversion and refinement, Seismol. Res. Lett. **87**, 964 (2016).

[44] R. Wu, P. A. Selvadurai, C. J. Chen, and O. Moradian, A FEM-based methodology to acquire broadband empirical Green's functions to understand characterization tests of acoustic emission sensors, Paper presented at the 54th U.S. Rock Mechanics/Geomechanics Symposium, physical event cancelled, June 2020.

[45] R. Wu, P. A. Selvadurai, C. Chen, and O. Moradian, Revisiting piezoelectric sensor calibration methods using elastodynamic body waves, J. Nondestruct. Eval. **40**, 68 (2021).

[46] K. Aki and P. G. Richards, *Quantitative Seismology* (University Science Books, 2002), p. 704.

[47] S. Stein and M. Wysession, *An Introduction to Seismology, Earthquakes, and Earth Structure* (John Wiley & Sons, New York, 2009).

[48] T. C. Hanks and H. Kanamori, A moment magnitude scale, J. Geophys. Res.: Solid Earth **84**, 2348 (1979).

[49] P. K. V. V. N. Mikko J. Alava and S. Zapperi, Statistical models of fracture, Adv. Phys. **55**, 349 (2006).

[50] A. Clauset, C. R. Shalizi, and M. E. J. Newman, Power-law distributions in empirical data, SIAM Rev. **51**, 661 (2009).

[51] J. D. Eshelby, The determination of the elastic field of an ellipsoidal inclusion, and related problems, Proc. R. Soc. London A **241**, 376 (1957).

[52] J. N. Brune, Tectonic stress and the spectra of seismic shear waves from earthquakes, J. Geophys. Res. **75**, 4997 (1970).

[53] W. R. Walter and J. N. Brune, Spectra of seismic radiation from a tensile crack, J. Geophys. Res. **98**, 4449 (1993).

[54] G. Mutke, A. Pierzyna, and A. Baranski, b-Value as a criterion for the evaluation of Rockburst Hazard in Coal Mines, in *Proceedings of the 3rd International Symposium on Mine Safety Science and Engineering* (McGill University Press, Montreal, Canada, 2016), pp. 1–5.

[55] G. Kwiatek, P. Martínez-Garzón, K. Plenkers, M. Leonhardt, A. Zang, S. von Specht, G. Dresen, and M. Bohnhoff, Insights into complex subdecimeter fracturing processes occurring during a water injection experiment at depth in Äspö Hard Rock Laboratory, Sweden, J. Geophys. Res.: Solid Earth **123**, 6616 (2018).

[56] L. Villiger, V. S. Gischig, J. Doetsch, H. Krietsch, N. O. Dutler, M. Jalali, B. Valley, P. A. Selvadurai, A. Mignan, K. Plenkers, D. Giardini, F. Amann, and S. Wiemer, Influence of reservoir geology on seismic response during decameter-scale hydraulic stimulations in crystalline rock, Solid Earth **11**, 627 (2020).

[57] J. Weiss, The role of attenuation on acoustic emission amplitude distributions and b-values, Bull. Seismol. Soc. Am. **87**, 1362 (1997).

[58] X. Liu, M. Han, W. He, X. Li, and D. Chen, A new b value estimation method in rock acoustic emission testing, J. Geophys. Res.: Solid Earth **125**, e2020JB019658 (2020).

[59] D. Chen, X. Liu, W. He, C. Xia, F. Gong, X. Li, and X. Cao, Effect of attenuation on amplitude distribution and b value in rock acoustic emission tests, Geophys. J. Int. **229**, 933 (2021).

[60] T. Utsu, Y. Ogata, R. S, and Matsu'ura, The centenary of the Omori formula for a decay law of aftershock activity, J. Phys. Earth **43**, 1 (1995).

[61] S. Lennartz-Sassinek, I. G. Main, M. Zaiser, and C. C. Graham, Acceleration and localization of subcritical crack growth in a natural composite material, Phys. Rev. E **90**, 052401 (2014).

[62] J. Davidsen, T. Goebel, G. Kwiatek, S. Stanchits, J. Baró, and G. Dresen, What controls the presence and characteristics of aftershocks in rock rracture in the lab? J. Geophys. Res.: Solid Earth **126**, e2021JB022539 (2021).

[63] M. N. Toksöz, D. H. Johnston, and A. Timur, Attenuation of seismic waves in dry and saturated rocks: I. Laboratory measurements, Geophysics **44**, 681 (1979).

[64] R. Wu, P. A. Selvadurai, Y. Li, Y. Sun, K. Leith, and S. Loew, Laboratory acousto-mechanical study into moisture-induced changes of elastic properties in intact granite, Int. J. Rock Mech. Min. Sci. **170**, 105511 (2023).

[65] R. Wu, P. A. Selvadurai, Y. Li, K. Leith, Q. Lei, and S. Loew, Laboratory acousto-mechanical study into moisture-induced reduction of fracture stiffness in granite, Geophys. Res. Lett. **50**, e2023GL105725 (2023).

[66] F. Birch, The velocity of compressional waves in rocks to 10 kilobars: 1, J. Geophys. Res. (1896-1977) **65**, 1083 (1960).

[67] J. Zemanek, Jr. and I. Rudnick, Attenuation and dispersion of elastic waves in a cylindrical bar, J. Acoust. Soc. Am. **33**, 1283 (1961).

[68] E. Langford, Quartiles in elementary statistics, J. Stat. Educ. **14** (2006).

[69] R. J. Oosterbaan, Frequency and regression analysis of hydrologic data, *Drainage Principles and Applications, Publication*, edited by H. P. Ritzema, 2nd Revised Edition, International Institute for Land Reclamation and Improvement (ILRI), (Wageningen, 1994).